Structural Dynamics of Myoglobin: FTIR-TDS Study of NO Migration and Binding†

Karin Nienhaus,‡ Pasquale Palladino,‡ and G. Ulrich Nienhaus*,‡,§

Institute of Biophysics, University of Ulm, Albert-Einstein-Allee 11, 89081 Ulm, Germany, and Department of Physics, University of Illinois at Urbana-Champaign, 1110 W. Green Street, Urbana, Il 61801

Received September 23, 2007; Revised Manuscript Received November 11, 2007

ABSTRACT: By using Fourier transform infrared photolysis difference spectroscopy combined with temperature derivative spectroscopy at cryogenic temperatures, we have measured infrared spectra of the stretching absorption on nitric oxide (NO) in the heme-bound and photodissociated states of ferrous and ferric nitrosyl myoglobin (MbNO) and a few site-specific Mb mutants. The NO absorption was utilized as a sensitive local probe of ligand interactions with active-site residues and movements within the protein. By comparison with results obtained in previous spectroscopic and structural studies of carbonmonoxy myoglobin (MbCO), the MbNO data were interpreted in structural terms. In the NO-bound state, conformational heterogeneity was inferred from the appearance of multiple bands, arising from different electrostatic interactions with active site residues, most importantly, His-64. In ferrous MbNO, a primary photoproduct site similar to site B of MbCO was found, as indicated by a characteristic NO stretching spectrum. In ferric MbNO, the His-64 side chain appears to interfere with trapping of NO in this site; only a very weak photoproduct spectrum was observed in Mb variants in which His-64 was present. Upon extended illumination, the photoproduct spectrum changed in a characteristic way, indicating that NO readily migrates to a secondary docking site C, the Xe4 cavity, in which the ligand performs librational motions on the picosecond time scale. This docking site may play a role in the physiological NO scavenging reaction. Surprisingly, NO cannot be trapped at all in secondary docking site D, the Xe1 cavity.

Nitric oxide (NO) has been recognized as a key biological messenger involved in a variety of physiological functions, including neurotransmission, regulation of blood pressure, prevention of platelet aggregation, and inhibition of vascular smooth muscle proliferation. Much of NO's biological functionality derives from its interactions with heme proteins. NO synthase enzymes exploit the unique chemical properties of the iron protoporphyrin IX group to produce NO. Binding of NO to the heme group of soluble guanylate cyclase leads to the production of the second messenger cyclic guanosine monophosphate from guanosine triphosphate (*1*, *2*). Another target of NO is cytochrome c oxidase, the terminal enzyme of the respiratory chain. Already nanomolar NO concentrations suffice to compete with O_2 for the binding site, thereby affecting apoptosis via the mitochondrial pathway (*3*). The reaction between NO and hemoglobin (Hb) is involved in intravascular NO homeostasis (*4*). Recently, myoglobin (Mb)[1] has been identified as an important NO scavenger that plays a crucial role in regulating NO levels within the cell (*5*−*7*).

The NO scavenging reaction of Mb involves multiple steps. Initially, the oxygenated ferrous (Fe^{2+}) Mb (MbO_2) reacts irreversibly with NO to yield ferric (Fe^{3+}) Mb and nitrate (*8*, *9*). Thereby, NO is continuously degraded. Subsequently, the ferrous unligated (deoxy) Mb is recovered by metMb reductase and rebinds O_2. However, ferric Mb can also bind NO and then react with another NO molecule to yield ferrous MbNO, which is a dead-end compound that can no longer take part in NO scavenging. Brunori has recently proposed that the temporary sequestration of NO in protein internal cavities may enhance the efficiency of the reaction because the spatial proximity would allow multiple collisions of NO with the FeO_2 moiety (*7*, *10*). This suggestion was based on detailed spectroscopic and crystallographic studies that provided evidence of migration of carbon monoxide (CO) and dioxygen (O_2) among internal cavities of Mb (*11*−*23*). Much less is known about the dynamics of NO within Mb (*24*−*27*), mainly due to the extremely high reactivity of the heme iron toward NO. Consequently, upon photolysis, essentially all NO ligands rebind geminately within picoseconds in ferrous MbNO (*27*−*32*); in ferric MbNO, the geminate process extends to the nanosecond time scale (*33*).

To explore the interactions of NO with Mb in detail, we have studied the NO stretching vibration in the infrared (IR) at cryogenic temperatures using Fourier transform IR (FTIR) photolysis difference spectroscopy in combination with temperature derivative spectroscopy (TDS). Previously, this sensitive technique allowed us to utilize CO as a local probe

† This work was supported by the Deutsche Forschungsgemeinschaft (grant no. 291/3) and the Fonds der Chemischen Industrie.

* Author to whom correspondence should be addressed. Tel. +49 731 5023050; fax +49 731 5023059; e-mail: uli@uiuc.edu.

‡ University of Ulm.

§ University of Illinois at Urbana-Champaign.

[1] Abbreviations: Mb, myoglobin; MbCO, CO-ligated Mb; $Mb^{II}NO$, ferrous NO-ligated Mb; $Mb^{III}NO$, ferric NO-ligated Mb; FTIR, Fourier transform infrared; TDS, temperature derivative spectroscopy

10.1021/bi701935v CCC: $40.75
Published on Web 12/28/2007

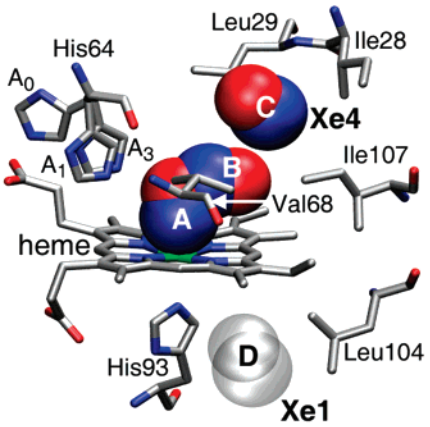

FIGURE 1: Structural model of wild-type Mb. Amino acid His-64 is shown in subconformations A_0, A_1, and A_3, as determined for MbCO (pdb code 1A6G (*60*)). A ligand is depicted bound to the heme iron (A), in the primary docking site B and in secondary sites C (Xe4) and D (Xe1).

within heme proteins, as the CO stretching absorption is fine-tuned by interactions with the environment and, therefore, provides detailed information on active-site conformations, effects of mutations and ligand docking sites (*11*, *16*, *17*, *34*−*37*). Measurements of the NO stretching vibration are more challenging, however, because of its weaker intrinsic absorption cross-section, spectral overlap with the amide bands in the case of NO bound to ferrous heme proteins, and incomplete NO photodissociation.

The experiments reported here were performed on wild-type MbNO and a variety of Mb mutants in both their ferric and ferrous forms. In the mutants, bulky amino acid side chains were introduced that were previously shown to block ligand passageways between protein internal cavities or fill these sites in MbCO at cryogenic temperatures (*11*). In wild-type MbCO, the primary docking site B close to the heme iron and secondary sites C and D sites (the Xe4 and Xe1 cavities (*38*), respectively) are accessible to the ligand (Figure 1). In mutant I28W, the bulky indole side chain of Trp-28 largely hinders access to site C, whereas Trp-104 completely blocks site D in mutant L104W. CO migration to both C and D is suppressed by an aromatic amino acid at position 68, as in mutant V68Y (*17*). At position 29, however, an aromatic residue enhances CO trapping in sites C and D, as has been observed for double mutant L29W-S108L (*16*, *39*) and triple mutant YQR (L29Y-H64Q-V67R) (*19*, *36*). To examine the interactions between NO and protein residues in the bound state and the primary photoproduct B, we have further included mutants H64L and H64V in this study, in which the key residue His-64, the distal histidine, is replaced by aliphatic amino acids. For both ferrous and ferric MbNO, multiple discrete protein conformations and multiple photoproduct states were characterized. Comparison with MbCO reveals similarities, but also distinct differences between the NO and CO dynamics within Mb. These results may form the basis for further detailed studies of the variety of NO-binding heme proteins.

MATERIALS AND METHODS

Preparation of Protein Samples. Mutants of sperm whale Mb were expressed in *Escherichia coli* strain Tb1 and purified as described (*40*). Excess potassium ferrocyanide was added to oxidize the protein material and subsequently removed by gel filtration. Ferrous NO-ligated samples (Mb^{II}-NO) were prepared in 75%/25% (by volume) glycerol/deuterated buffer (1 M potassium phosphate in D_2O). After dissolving the protein to a final concentration of 20 mM, the sample solution was equilibrated with N_2 gas for 1 h. A twofold molar excess of anaerobically prepared sodium dithionite solution (in D_2O) was added, followed by a twofold molar excess of anaerobically prepared sodium nitrite solution (in D_2O). $Na^{14}NO_2$ and $Na^{15}NO_2$ isotopes were used to aid in IR band assignment.

Ferric NO samples ($Mb^{III}NO$) were obtained by dissolving the oxidized protein at a concentration of 30 mM in 1 M phosphate buffer. The solution was stirred under N_2 for 1 h in a gastight vessel to remove any dissolved O_2. The deaerated solution was exposed briefly (∼5 min) to a 1:9 mixture of NO/N_2 gas at 1 bar, while the progress of the binding reaction was constantly monitored by UV/visible spectroscopy. Special precautions were taken to avoid reductive nitrosylation of the heme iron: As soon as ∼30% of the protein molecules were ligated, degassed glycerol was added to a final concentration of 50% (by volume), and subsequently the NO atmosphere above the sample was replaced by N_2 to terminate the reaction. Prior to data collection with $Mb^{III}NO$ samples of optimal path length (75 μm), each preparation was checked for possible contamination with ferrous protein by taking FTIR spectra on a thin sample (5−10 μm), so that the stretching vibration of ferrous heme-bound NO (∼1600 cm^{-1}) could be observed in the presence of the strongly absorbing amide vibrations of the protein.

For all samples, pH values were determined at ambient temperature with a commercial H_2O-calibrated pH meter and are quoted as measured. Note that the pD value is actually 0.45 pH units higher (*41*). We have refrained from a pH/pD recalibration because a fraction of the protons of the protein will exchange with deuterons from the solvent, and moreover, temperature has a pronounced effect on the pKs of protonatable amino acids (*42*). A well-studied example is His-64 of MbCO, for which a temperature change from 290 to 180 K results in an apparent p*K* increase by ∼1.2 pH units in 75%/25% (by volume) glycerol/buffer solution (*43*).

FTIR Spectroscopy. All sample solutions were centrifuged at 5000 rpm for 15 min prior to loading to remove any undissolved or aggregated material. A few microliters of sample solution were placed between two CaF_2 windows (diameter 25.4 mm) separated by a 5−75 μm thick mylar washer, depending on the desired path length. The samples were kept in a cryostat with a precise temperature control system as described previously (*44*). FTIR transmission spectra were collected either with the external MCT detector (resolution 2 cm^{-1}, range 1000−4000 cm^{-1}) or the InSb detector (resolution 2 cm^{-1}, range 1700−2300 cm^{-1}) of an IFS 66v/S FTIR spectrometer (Bruker, Karlsruhe, Germany). For photolysis, the samples were exposed to 532-nm laser light from a frequency-doubled Nd:YAG laser delivering 300 mW (model Forte 530−300, Laser Quantum, Manchester, UK).

Temperature Derivative Spectroscopy (*TDS*). This temperature ramp protocol allows thermally activated rate processes to be studied that are characterized by static distributions of enthalpy barriers (*43*, *45*, *46*). These distribu-

tions are universally observed in kinetic experiments on proteins at cryogenic temperatures and are a result of conformational heterogeneity of the protein ensemble (*47*, *48*). In a first step, the sample is photolyzed by exposure to 532-nm laser light. Two different illumination protocols were employed that are known to generate different photoproduct populations in MbCO: (i) short-term illumination at 4 K (CO ligand: 1 s; NO ligand: 20 s, see below), upon which photolyzed ligands preferentially settle in the primary docking site B (*11*, *49*), and (ii) slow cooling from 160 to 4 K over several hours (cooling rate 0.3 K/min) while continuously illuminating the sample, which is an efficient way to populate secondary transient docking sites C and D (*11*, *17*, *46*, *50*). Immediately after photodissociation, the sample temperature is increased at a rate of 0.3 K/min in the dark, and one FTIR transmission spectrum is recorded every Kelvin. Absorption difference spectra are calculated for successive temperatures, $A(\nu, T) = \log [I(\nu, T - 1/2\ \mathrm{K}) - I(\nu, T + 1/2\ \mathrm{K})]$, which approximates the negative derivative of the population with respect to temperature, $-\mathrm{d}N(T)/\mathrm{d}T$. In the simplest form of the TDS data analysis, one assumes that a change in the integrated absorbance (spectral area) is solely due to ligand rebinding, and the absorbance change is set proportional to the rebinding population, $\Delta A(\nu, T) \propto \Delta N(\nu, T)$. However, the IR bands of both heme-bound and photodissociated ligands often exhibit intrinsic temperature dependencies in their spectral positions, widths, and areas (*35*, *51*−*53*), which will all give rise to difference signals in the TDS data and may demand more complex data analyses.

RESULTS AND DISCUSSION

Conformational Heterogeneity at the Active Site of Myoglobin. Conformational Substates in MbCO. The CO derivative of Mb has become a paradigm in the study of structural heterogeneity and dynamics, largely due to the exquisite sensitivity of the IR stretching absorption of CO, which can be used as a local probe of its structural environment. In the heme-bound form, three CO stretching bands can be distinguished that arise from the presence of discrete bound-state conformations. These major substates, denoted as A_0, A_1, and A_3, are associated with IR bands at 1966, 1945, and 1930 cm^{-1}, respectively (*11*, *43*, *49*). The dispersion of the CO stretch absorption into a small number of A substate bands is caused by electrostatic interactions, mainly between the CO dipole and the imidazole side chain of His-64 (*54*−*57*). The side chain has a p*K* of 4.5 at room temperature (*56*). In the low-pH conformation A_0, the imidazole is protonated and rotated toward the solvent for better solvation of its charge, whereas it is neutral and resides in the distal pocket in the high-pH conformations A_1 and A_3 (*58*, *59*). X-ray structure analysis at 1.2 Å resolution (Figure 1) suggests that the His-64 imidazole is located more deeply in the heme pocket in A_3 than in A_1 (*60*). Thereby, it produces additional steric hindrance at the active site, which is reflected in a markedly higher enthalpy barrier against CO binding in A_3 (*61*). The variations in the stretching frequencies of heme-bound CO are described within the backbonding model (*62*). Positive partial charges in the vicinity of the CO oxygen lower its stretching frequency, whereas negative partial charges have the opposite effect (*63*). Electrostatic influences also play a role when the CO is dissociated from the heme iron and migrates within the protein. Vibrational Stark effects due to local electric fields give rise to characteristic spectra that allow ligand migration to and dynamics within a docking site to be analyzed in great detail (*51*, *52*).

$Mb^{II}NO$ Active Site Conformations. By using Raman spectroscopy, Coyle and co-workers (*64*) screened a large array of ferrous MbNO samples and found a linear correlation between the stretching frequencies of heme-bound NO and CO, with a slope of 0.92. This result implies that heme-bound NO in $Mb^{II}NO$ acts in a similar way as heme-bound CO as a local probe of the active site; the N−O bond is almost as sensitive to electrostatic fields at the binding site as the C−O bond, which is also consistent with the reported identical Stark tuning rate, $\Delta\mu \approx (2.4/f)\ \mathrm{cm}^{-1}/(\mathrm{MV/cm})$, found upon application of external electric fields for both ligands (*65*). Here, f is the local field correction factor estimated to be in the range 1.1−1.3.

We have calculated absorbance difference spectra of wild-type and mutant $Mb^{II}NO$ samples from transmission spectra before and after photolysis. For better comparison, all spectra in Figures 2 and 3 were normalized to equal areas. The stretching frequencies of the individual bands were determined by nonlinear least-squares fitting with multiple Gaussians and are compiled in Table 1. The spectra in the region of heme-bound NO are displayed in Figure 2A for mixed wild-type $Mb^{II}NO$/MbCO samples at four different pH values. The dominant conformation in wild-type $Mb^{II}NO$ at neutral pH is represented by the band at 1614 cm^{-1} and, by comparison with MbCO, should thus be similar to the A_1 conformation. Consequently, the shoulder at 1607 cm^{-1} may correspond to a conformation similar to A_3 in MbCO, with a stronger interaction between the ligand and the His-64 side chain, because it is located at a lower frequency with respect to A_1 (Figure 2A). However, the difference in the stretching frequency of the two substates is smaller for NO ($\Delta\nu = 7$ cm^{-1}) than for CO ($\Delta\nu = 15$ cm^{-1}), suggesting more similar interactions in the two states of $Mb^{II}NO$. For an ^{15}NO isotope sample, we expect a shift of the main band by 29 cm^{-1} to 1585 cm^{-1} on the basis of an NO reduced mass renormalization (red dotted line in Figure 2A). However, the ^{15}NO stretching spectrum at pH 7.3 displays two separate bands at 1581 and 1588 cm^{-1} that are blue-shifted by 1.0 cm^{-1} at pH 6 and pH 5.5. This splitting does not reflect conformational heterogeneity, as was suggested earlier (*24*), but arises from a Fermi resonance between the stretching modes of NO at 1585 cm^{-1} and Cβ-Cβ of the porphyrin ring at 1583 cm^{-1} (*66*, *67*).

The spectra of the I28W and L104W mutants closely resemble that of wild-type $Mb^{II}NO$, with large bands at 1614 and 1612 cm^{-1} and minor bands at 1604 and 1603 cm^{-1}, respectively (Figure 3A), indicating that the electrostatic interactions are local in nature and not affected by mutations remote from the active site. With respect to the wild-type protein, V68Y shows a strongly red-shifted doublet of bands at 1593 and 1582 cm^{-1} (Figure 3A). The better spectral separation of the small band from the main peak may also arise from the Fermi resonance mentioned above. A similar shift, although not as pronounced, has been observed for mutant V68F (*64*). The red-shift suggests that the edge of the aromatic π-electron system of Tyr-68 or Phe-68 places a positive partial charge in the vicinity of the ligand oxygen and thereby decreases the N−O bond order. Interestingly,

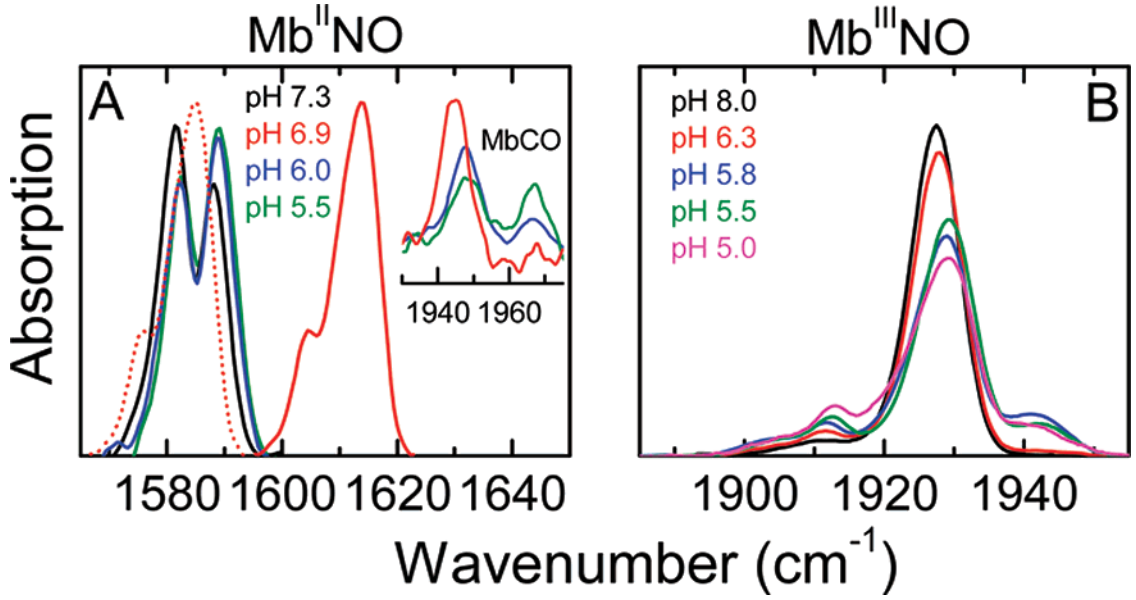

FIGURE 2: FTIR photolysis difference spectra of (A) ferrous and (B) ferric MbNO samples at 4 K at various pH values.

in V68Y MbCO, this red-shift is only on the order of 1 cm^{-1}, which indicates that NO interacts more strongly than CO with Tyr-68.

The spectra of the two distal histidine mutants H64L and H64V Mb^{II}NO display two huge bands at 1635 and 1638 cm^{-1} that are considerably blue-shifted from the A_1 conformation (Figure 3A). This qualitative behavior is expected upon removal of the interaction with His-64 (*54*, *55*, *63*). We have made substantial efforts to prepare wild-type Mb^{II}NO samples at low pH so as to populate an A_0-type substate, with a protonated His-64 removed from the distal heme pocket and a stretching band at ~1640 cm^{-1}, as reported from resonance Raman spectroscopy (*64*). However, our mixed CO/NO preparation at pH 5.5 did not show the slightest hint of an A_0-type band at higher frequency for Mb^{II}NO, although there was ~50% of A_0 populated in the MbCO fraction of the sample (inset Figure 2A). A mixed CO/NO L104W mutant sample containing ~60% of A_0 molecules in MbCO neither showed an A_0-type species (data not shown). Unfortunately, we did not succeed in preparing concentrated IR samples at pH <5.5 due to denaturation. Still, the data presented here provide clear evidence that the closed conformation, with the His-64 side chain inside the distal pocket, is energetically favored in the NO-ligated species with respect to CO, presumably because of a stronger hydrogen bond with His-64. We cannot exclude, however, that His-64 becomes protonated at Nδ but still retains its hydrogen bond between the hydrogen on Nϵ and the NO (although we would expect to see an NO band shift in this case).

Mb^{III}NO Active Site Conformations. As Mb^{III}NO is isoelectronic to MbCO, it is tempting to explain its spectra with the simple backbonding formalism as well (*62*, *63*). Indeed, the IR spectrum of wild-type Mb^{III}NO displays, depending on pH, up to three bands of heme-bound NO at 1914, 1927, and 1942 cm^{-1} that appear similar to the three 'canonical' substates A_3, A_1, and A_0 of MbCO (Figure 2B, Table 1). Closer inspection reveals that the band at 1914 cm^{-1} grows continuously upon lowering the pH, and an additional band appears at ~1902 cm^{-1}. The 1942-cm^{-1} band does not appear to have a systematic pH variation; it is very weak at pH 6.3 and 8. In I28W Mb^{III}NO (pH 6.5), there are three bands at 1917, 1928, and 1942 cm^{-1} (Figure 3D). At pH 5.6, only the band at 1917 cm^{-1} persists. The main absorption band of L104W Mb^{III}NO (pH 6.3) is located at 1924 cm^{-1}; a broad foot extends toward lower wavenumbers. At pH 4.6, the 1924-cm^{-1} band loses intensity and a new peak emerges at 1913 cm^{-1} (Figure 3D). Mutants H64L and V68Y display only single bands at 1901 and 1918 cm^{-1}, respectively.

To obtain insight into the structural properties of the different conformations, we note that the spectrum of H64L Mb^{III}NO exhibits only a single NO band at 1901 cm^{-1} (Figure 3D). Consequently, a band near this frequency would be assigned to an A_0-type substate, with a His-64 side chain that does not interact with the NO. However, all three bands in Mb^{III}NO are shifted to higher frequency, suggesting that a negative partial charge interacts with the heme-bound NO ligand in all three substates. To explain the band of the dominant species in Mb^{III}NO at 1927 cm^{-1}, we propose an interaction between the bound NO and the free electron pair of a deprotonated His-64-Nϵ in the alternative tautomeric state of the neutral His-64, in which Nδ is protonated, in agreement with Miller et al. (*24*).

To elucidate the conformations associated with the other NO stretching bands, Mb^{III}NO absorption spectra were determined at various pH values between pH 5 and 8 (Figure 2B). With decreasing pH, the low-frequency band at 1914 cm^{-1} increases in area, and a weak band appears at 1902 cm^{-1}. This latter feature could represent an A_0-type conformation, as its frequency is very close to 1901 cm^{-1}, the band position observed for H64L Mb^{III}NO. The nature of the band at 1914 cm^{-1} remains unclear, however. From the pH dependence, a possible assignment involves a protonated His-64 as well, where an additional water molecule residing in the distal pocket may cause an upshift of the 1902-cm^{-1} band. We note that the two low-frequency bands tentatively associated with a protonated His-64 still form a small fraction of the total population at pH 5 at 4 K, whereas A_0 clearly is a majority species in MbCO at this pH (see inset in Figure 2A). A similar behavior was already discussed above for

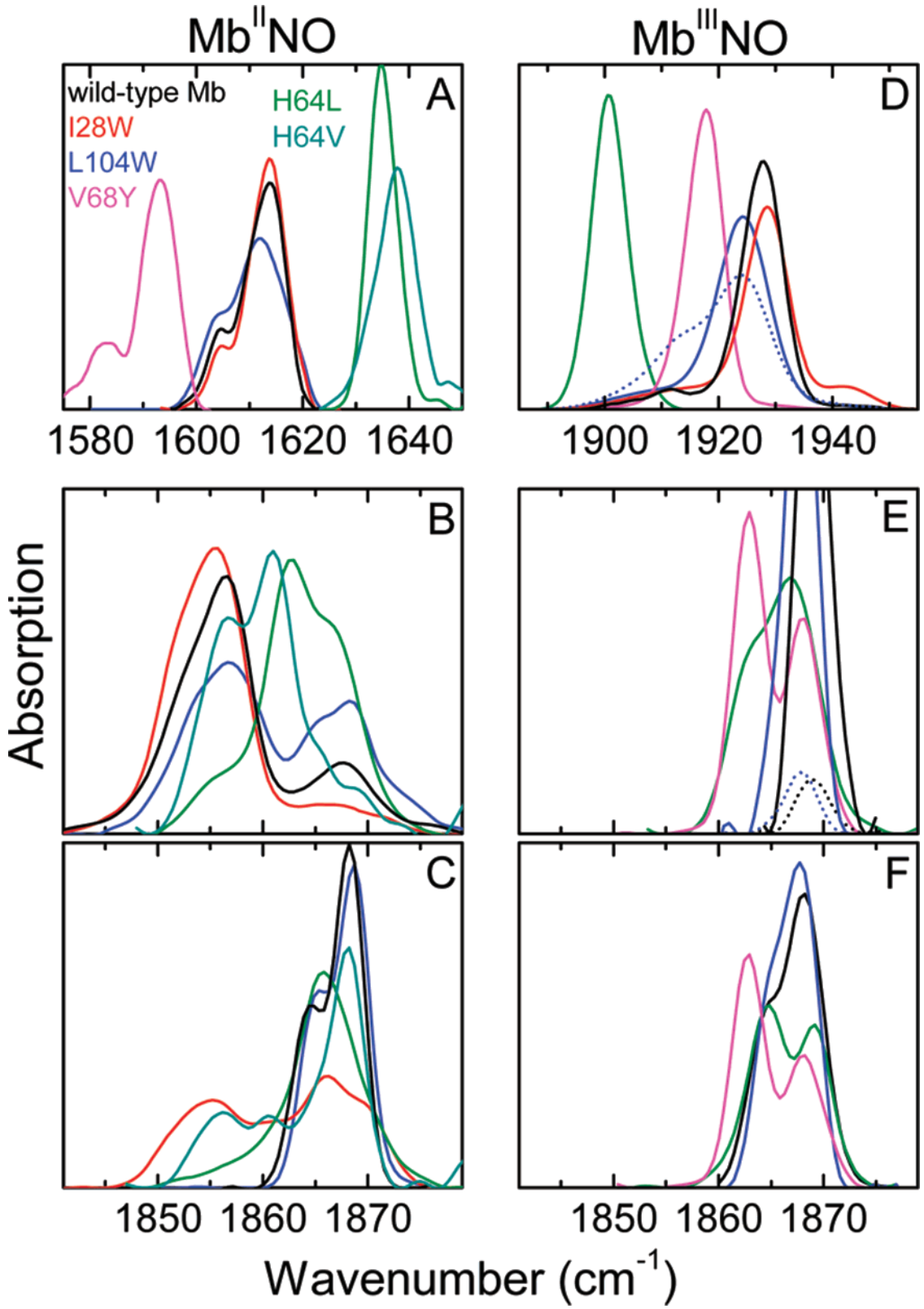

FIGURE 3: FTIR photolysis difference spectra of (left column) ferrous and (right column) ferric MbNO samples at 4 K. (A, D) NO bound to wild-type and select mutant Mb samples, photoproduct spectra measured (B, E) after 20-s illumination at 4 K and (C, F) after slow cooling from 160 to 4 K under light.

$Mb^{II}NO$. This observation suggests that the electrostatic interaction between His-64-Nϵ and NO prevents protonation and causes a downshift of the p*K* of His-64. We were unable to prepare samples at lower pH due to denaturation, so that we could not study the pH dependence of these species more closely.

The band at 1942 cm^{-1} exhibits the highest frequency and therefore should be assigned to a species similar to the one at 1927 cm^{-1} but with an even stronger interaction between the bound NO and the lone electron pair on His-64-Nϵ. This assignment, which is analogous to the one proposed for the A_1 and A_3 substates of MbCO, is further supported by the

Table 1: Band Positions of the IR Stretching Absorption of Heme-Bound and Photodissociated CO and NO Ligands in Wild-Type and Mutant Mb Samples. Band Positions Were Determined at 4 K, with an Estimated Experimental Error of ±0.5 cm^{-1}

	ν(heme-bound ligand) (cm^{-1})			ν(photolyzed CO) (cm^{-1})		ν(Fe^{III}photolyzed NO) (cm^{-1})		ν(Fe^{II}photolyzed NO) (cm^{-1})	
Mb sample	MbCO	$Mb^{III}N O$	$Mb^{II}N O$	B	C	B	C	B	C
wild-type Mb									
pH	7.0	8.0	6.9						
A_3	1930	1942?	1607	2149					
A_1	1945	1927	1614	2119 2131	2132	–	1865 1869	1852 1857	1865 1869
A_0	1965	1914							
H64L									
pH	6.8	7.0							
A_0	1965	1901	1635	2126	2132 2136	1862 1867	1864 1869	1862 1867	1865 1869
H64V									
pH	7.1		7.3						
A_0	1968		1638	2124 2129				1857 1861	1869
I28W									
pH	7.2		7.2						
A_3	1929	1942?	1605	–				–	–
A_1	1945	1928	1614	2118 2131		-	1865 1869	1852 1856	1865 1869
A_0		1917							
L104W									
pH	7.3	6.3/4.6	7.1						
A_3	1932	1934	1603	2149					
A_1	1944	1924/1924	1612	2118 2131	2132	–	1865 1869	1852 1857	1865 1869
A_0		1912/1913							
V68Y									
pH	7.2	6.0	7.3						
A_3	1931	1918	1582	2107 2150		1863 1868	not occupied	ND	ND
A_1	1944		1593	2111 2139					
A_0	1961								
L29W-S108L									
pH	7.6	7.3	7.2						
A_I	1945	1932	1604	2122 2131	2124 2137	–	1865 1869	–	1865 1869
A_{II}	1965	1906 1917	1609						

TDS experiments on $Mb^{III}NO$ (see below). This substate has a comparatively high peak rebinding temperature of ~40 K, as compared to 15 K for the dominant population at 1927 cm^{-1}, which suggests that His-64 poses a significant rebinding barrier in this conformation. Because of the spectral closeness of the band at 1942 cm^{-1} on $Mb^{III}NO$ and the A_1 substate band of MbCO at 1945 cm^{-1}, we have also entertained the idea that the band at 1942 cm^{-1} may arise from a small fraction of MbCO. However, the frequencies clearly differ by 3 cm^{-1}, and the maximum rebinding temperature of CO in the A_1 substate band of MbCO is 50 K and not 40 K as observed here (see below). To aid in the assignment of this band, we had expected to obtain information from a V68Y $Mb^{III}NO$ sample, which is known to have ~70% (30%) of the V68Y molecules in the A_3 (A_1) conformation in MbCO (*17*). However, the spectrum of V68Y $Mb^{III}NO$ shows only a single A substate band at 1918 cm^{-1} (Figure 3D), which suggests that Tyr-68 causes a weakening of the interaction between NO and His-64, forcing the His-64 imidazole away from the ligand. Further evidence of this scenario will be given below in the discussion of the photoproducts. Alternatively, Tyr-68 could compensate for part of the shift induced by His-64 by contributing a positive partial charge, similar to what was already proposed for Mb^{II}-NO.

To summarize, active site heterogeneity exists in ferrous and ferric NO-ligated Mb that resembles the phenomena observed for MbCO. In each oxidation state, several substates can be distinguished on the basis of the stretching bands of the heme-bound NO. The comparison of active-site mutants shows that, as in MbCO, His-64 plays a key role in the noncovalent interactions also with the NO ligands; the pH dependence of the spectral changes indicates that these interactions are stronger than with CO. With the exception of the substate related to the band at 1942 cm^{-1} in $Mb^{III}NO$, His-64 does not make an appreciable contribution to the rebinding enthalpy barrier in any of the conformations of NO-ligated Mb.

Ligand Dynamics in Photodissociated MbNO. Formation and Yield of Photoproducts. The FTIR-TDS technique relies on the photolability of the ligand−iron bond and the presence of specific docking sites in which the ligands become trapped and can be identified by a characteristic spectroscopic signature. To establish an efficient photolysis protocol for NO-ligated Mb, mixed $Mb^{II}NO$/MbCO and $Mb^{III}NO$/MbCO samples of mutant H64L, with path lengths of 25 and 75 μm, respectively, were prepared and illuminated at 4 K. The laser intensity was attenuated 1000-fold by using a 3-OD neutral density filter. These mixed preparations enable a direct comparison of the NO and CO photolysis yields because simultaneous measurement of CO and NO spectra cancels effects because of laser power and sample density variations. Mutant H64L was chosen here because, in contrast to wild-type Mb, the absorption bands of heme-bound CO and NO do not overlap in H64L $Mb^{III}NO$/MbCO (Figure 2). Transmission spectra were collected continuously during illumination and referenced against a transmission spectrum taken in the dark. The photoproduct yields were determined from the photolysis-induced decrease of the absorption bands of heme-bound NO and CO and plotted as a function of the illumination time in Figure 4. The prepared photoproduct

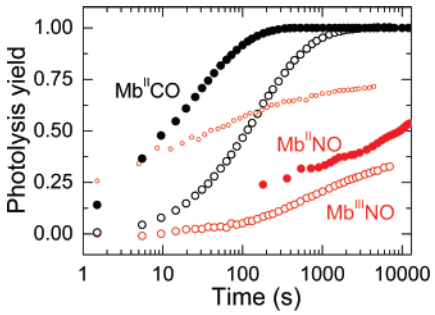

FIGURE 4: Photolysis yields of H64L MbCO (black symbols), Mb^{II}NO (red, closed symbols) and Mb^{III}NO (red, open symbols; small symbols: full laser power) upon constant laser illumination through a 3-OD neutral density filter at 4 K, calculated from the decrease of the absorption bands of the heme-bound ligand.

states did not recombine during several hours in the dark at 4 K, as expected.

Figure 4 shows that trapping in a photoproduct site after photodissociation is much more efficient for CO than for NO. It takes ~1000 s to completely photodissociate MbCO and hence ~1 s without the 3-OD filter. In some mutants, subsequent illumination for many hours can provide energy to the CO in site B so that it may migrate to other sites with higher barriers against rebinding even at 4 K (*16*). Alternatively, CO ligands have been observed to explore alternative docking sites upon raising the temperature after photolysis at 4 K (*36*). Furthermore, efficient CO migration to alternative sites can be induced by continuous illumination while slowly cooling the sample, for instance, from 160−4 K (*46*, *50*). Formation of photoproducts takes much longer in both ferric and ferrous MbNO than in MbCO. For Mb^{II}NO and also Mb^{III}NO, the quantum yield of photolysis is 0.5−1 (*30*, *68*, *69*). Consequently, the much slower response to photolysis light at 4 K indicates that most ligand trajectories terminate in the bound state right after photodissociation. Essentially complete photolysis of NO is achievable but requires many hours of continuous illumination with full laser power (Figure 4, small open symbols). High photolysis yields can be obtained using slow-cool illumination that efficiently traps the NO ligands in remote sites.

Meuwly and co-workers have proposed that photolysis of NO-bound Mb at cryogenic temperatures may lead to the formation of both ferric (*70*) and ferrous (*71*) Fe−ON complexes. Such metastable species have been reported upon photolysis of iron nitrosyl porphyrins at 25 K (*72*). We have taken great care not to overlook any photolysis-induced spectral changes that could be assigned to Fe−ON photoproducts in the entire spectral range in which they may be expected. However, we only found the typical photoproduct absorption bands associated with 'free NO' in the protein between 1840 and 1880 cm^{-1} even after extended photolysis (Figure 3).

Primary Photoproduct of Mb^{II}NO. After brief illumination of MbCO at 4 K, the photolyzed ligands are trapped in the primary docking site B, in which the CO is located on top of pyrrole ring C of the heme group (*73*−*76*). In the A_1 conformation, two CO stretching bands are observed at 2119 and 2131 cm^{-1}; they are associated with opposite orientations of the ligand at site B. The doublet arises from vibrational Stark splitting, i.e., from interactions between the CO dipole and the local electric field at the docking site (*74*, *77*, *78*). As for the A substate bands, the interaction with the His-64 side chain is the main determinant of the CO stretching frequency (*78*). The photoproduct spectra of I28W, L104W, and wild-type MbCO are very similar (Table 1) because all these proteins have an identical active site structure and hence the same electric field at site B (*11*). The larger Stark splitting of the CO bands at site B for the A_3 than the A_1 substate of MbCO (*79*) points to a decreased distance between the photolyzed ligand and the His-64 side chain (*60*).

Because the majority population of wild-type sperm whale Mb^{II}NO is associated with the band at 1614 cm^{-1}, the photoproduct spectrum in Figure 3B obtained after 20-s illumination at 4 K is essentially governed by this species. Its integrated area is ~20× smaller than the one of heme-bound NO. It displays a doublet of bands, a large peak at 1857 cm^{-1}, and a smaller one at 1867 cm^{-1}. A shoulder at 1852 cm^{-1} is also apparent. The main photoproduct band of the ^{15}NO wild-type Mb^{II}NO sample is centered at 1824 cm^{-1}, with a small shoulder at 1820 cm^{-1}; the minor peak is seen at 1834 cm^{-1} (data not shown). For mutants I28W and L104W, the spectra of the ferrous state look qualitatively similar; however, the high-frequency component 1867 cm^{-1} is weaker in I28W and stronger in L104W than in wild-type Mb^{II}NO (Figure 3B, Table 1). In L104W, a further splitting into two bands at 1865 and 1869 cm^{-1} is evident. Incidentally, Miller et al. (*24*) also identified the two bands at 1852 and 1857 cm^{-1} in horse heart Mb^{II}NO, where they appeared spectrally better resolved. A weak band at 1869 cm^{-1} is also visible in their data. Consequently, all spectra show a splitting of bands by ~10 cm^{-1}, with a large population at 1857 cm^{-1} and a minor one at 1867 cm^{-1}. It appears that even mutations remote from the active site can influence the ratio of the two components in a rather subtle way, as was previously noticed for MbCO (*11*). In addition, these bands are further split by 4−5 cm^{-1}, at least in the low-frequency component of all spectra. For the high-frequency component, this additional splitting is only clearly visible for the L104W mutant. In the aliphatic mutants H64V and H64L, we have observed essentially only two bands split by 5 cm^{-1}; they are located in between the more strongly split bands of samples containing His-64 (Figure 3B). Therefore, we suggest that the large splitting arises from an electrostatic interaction between His-64 and the NO in two different orientations in the primary docking site B, very similar to the situation in MbCO.

This assignment is further supported by an estimation of the extent of splitting expected for NO in photoproduct site B. The frequency shift, $\Delta\nu$, of a vibrational transition dipole that is oriented at an angle θ with respect to a local field E_{int} can be computed as

$$h\Delta\nu = -|\vec{\Delta}\mu||E_{int}|\cos\theta \qquad (1)$$

where $|\Delta\vec{\mu}|$ is called the Stark tuning rate, which has its physical origin in bond anharmonicity and electronic polarizability (*65*). For CO in frozen 2-methyltetrahydrofuran, a Stark tuning rate of 0.43 cm^{-1}/(MV/cm) has been determined experimentally (*80*). For noncovalently bound or free NO, to our best knowledge, Stark tuning rates have not yet been measured. Recent ab initio DFT calculations have predicted Stark tuning rates of 0.36 cm^{-1}/(MV/cm) for NO and 0.51 cm^{-1}/(MV/cm) for CO (*81*). Stark tuning rates of 0.53 and

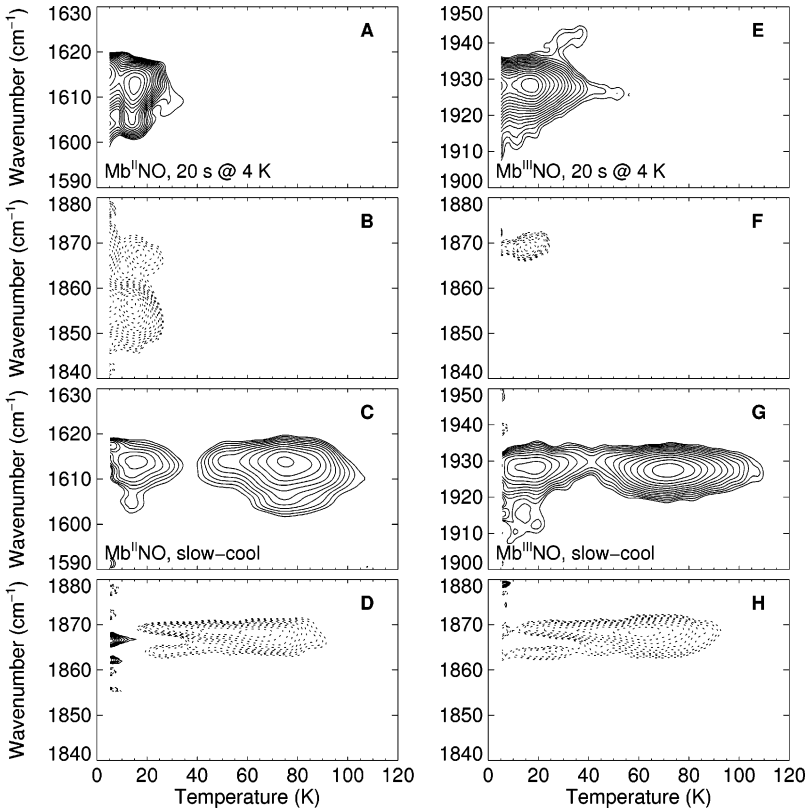

FIGURE 5: TDS contour maps of (left column) Mb^{II}NO and (right column) Mb^{III}NO; contours are spaced logarithmically. The maps show temperature dependent absorption changes of (A, E) heme-bound and (B, F) photodissociated NO after 20-s illumination at 4 K, and (C, G) heme-bound and (D, H) photodissociated NO after slow cooling from 160 to 4 K under continuous illumination. Solid and dotted lines represent absorption increases and decreases, respectively.

0.63 cm^{-1}/(MV/cm) have been obtained by using classical electrostatics, treating ligand binding as 'electrostatic bond formation' (*82*). These calculations are in semiquantitative agreement with our assignments, indicating that the Stark splitting is somewhat smaller for NO than for CO (10 versus 12 cm^{-1}) at site B in ferrous wild-type Mb at 4 K. This interpretation, however, still leaves the observed additional splitting by 4−5 cm^{-1} to be explained. For samples in which His-64 is present, the splitting could originate from the two bound-state conformations at 1607 and 1614 cm^{-1} that generate two doublets, as for A_1 and A_3 of MbCO (*79*). Alternatively, additional NO orientations in the primary docking site could also produce these bands. H64L and H64V Mb^{II}NO exhibit only single bound-state bands, so that heterogeneity in the ligand-bound conformation can be excluded. Even for CO in photoproduct site B, a splitting exists in these mutants (4.5 cm^{-1} in H64V (*54*)). Likely, the splitting is produced by the remaining electric field in the absence of His-64. The presence of water molecules in the distal pocket at low temperature upon removal of the imidazole moiety could also be responsible for more complicated IR spectra (*83*).

Primary Photoproduct of Mb^{III}NO. After brief illumination of the ferric wild-type protein, a significant fraction is photodissociated, as inferred from the bands of heme-bound NO, but stretching bands related to photoproduct species are essentially absent in the region around 1850 cm^{-1}, as was reported earlier (*24*). We made the same observation for mutant L104W. Close inspection revealed an extremely weak, single band at 1869 cm^{-1} (Figure 3E), with an area that is ~160× smaller than that of the bound-state bands. In Figure 3E, the dotted black and blue lines indicate the actual amplitudes of the bands with respect to the other photoproduct bands. In mutant I28W, despite a thorough search in the entire spectral range, we were unable to find any bands that may be assignable to the NO ligand stretching vibration. From the TDS map in Figure 5F (see below), it is evident that this absorption arises from NO molecules rebinding at low temperature (<25 K) and not from those that have escaped to secondary binding sites. Moreover, the spectrum is distinctly different from the one of Mb^{II}NO, which excludes an explanation involving a small contamination with the ferrous species. Therefore, we believe that only a small fraction of the NO molecules docks in a specific site in the distal pocket so that it gives rise to a well-defined absorption band. We emphasize that we have carefully scanned the entire frequency range in which NO or even NO^+ ($\nu \approx 2300$ cm^{-1} (*84*)) may absorb.

In contrast to wild-type and L104W, H64L Mb^{III}NO again displays a stretching spectrum of photodissociated NO, with an integrated absorbance 25-fold lower than that of bound NO, showing two bands at 1862 and 1867 cm^{-1} (Figure 3E). The band positions are identical to those seen for the ferrous sample. Apparently, NO in the primary photoproduct site of H64L Mb^{III}NO is insensitive to the oxidation state of the heme iron. The reappearance of photoproduct bands in the absence of His-64 indicates that its presence in wild-type Mb^{III}NO precludes docking of photodissociated NO ligands. Interestingly, 20-s illumination of V68Y Mb^{III}NO yields a photoproduct doublet at 1863/1868 cm^{-1} (Figure 3E), suggesting that there is no significant interaction between the His-64 side chain and the photolyzed NO in this mutant.

From the rather low frequency of the heme-bound NO (1918 cm^{-1}), we had already inferred that the bulky Tyr-68 side chain forces the His-64 imidazole away from the ligand. On the basis of these observations, His-64 in ferric wild-type Mb essentially prevents trapping of NO ligands in the primary docking site B in well-defined orientations. As a result, the NO ligands give rise to a very broad stretching absorption that cannot be distinguished from the background.

NO Migration to Remote Photoproduct Sites. After slow cooling from 160 to 4 K under continuous illumination, photoproduct spectra of ferrous wild-type and mutant samples (Figure 3C) are very different from those after brief illumination (Figure 3B). Essentially identical spectra are obtained for wild-type and L104W $Mb^{II}NO$; they are dominated by a doublet at 1865 and 1869 cm^{-1}. In mutant I28W, the two doublets at 1852/1857 cm^{-1} and 1865/1869 cm^{-1} contribute roughly equally to the overall spectral area. The spectrum of H64L $Mb^{II}NO$ shows a single, rather broad band at ~1865 cm^{-1}, whereas a new large peak appears at 1869 cm^{-1} in H64V in addition to the two bands at 1857 and 1861 cm^{-1} that were already present after brief illumination.

For wild-type and L104W $Mb^{III}NO$, slow cooling under continuous illumination from 160 to 4 K again yielded easily measurable photoproduct spectra, with spectral areas ~20-fold smaller than those of the bound-state spectra. They display the same 1865/1869-cm^{-1} doublet that was already observed in the ferrous samples (Figure 3F). This doublet is also present in the spectrum of mutant H64L after slow-cool illumination. Still no photoproduct bands were found for I28W, whereas the photoproduct spectra after brief and prolonged illumination of V68Y are identical.

NO Rebinding from the Primary Docking Site. To examine the rebinding behavior of NO from the photoproduct states created by the different photolysis protocols, TDS experiments were started immediately after 20-s illumination and, in addition, also after slow cooling under light from 160 to 4 K. The TDS data of wild-type MbNO are shown in Figure 5 as logarithmically scaled contour plots of the absorption changes on a surface spanned by the wavenumber and temperature axes; solid and dotted lines represent increasing and decreasing absorption, respectively.

After 20-s illumination, rebinding in both the major (1614 cm^{-1}) and the minor (1607 cm^{-1}) conformations of Mb^{II}-NO occurs mainly at 15 K (Figure 5A). The decrease of the photoproduct bands at 1852, 1857, and 1867 cm^{-1} is also maximal at 15 K (Figure 5B). For wild-type $Mb^{III}NO$, maximum rebinding occurs at 15 K in the bands at 1924 and 1914 cm^{-1} and at 40 K in the band at 1942 cm^{-1} after brief illumination (Figure 5E). A weak tail in the contours of the dominant band extends up to 60 K, which indicates that a very small fraction of NO ligands has already escaped to the remote site during illumination. The signal in the photoproduct map (Figure 5F) is extremely weak and localized below 25 K.

In MbCO, the enthalpy barriers that govern rebinding from the primary docking site B are markedly different for the three A substates. For example, the peak enthalpies of A_1 and A_3 are 10.1 and 19.5 kJ/mol, respectively (*61*), which suggests that the His-64 side chain exerts more steric hindrance in A_3. For wild-type $Mb^{II}NO$, however, the two conformations related to A_1 and A_3 behave identically with respect to NO rebinding in the FTIR-TDS experiments, in agreement with kinetic studies of Miller et al. (*24*). Recombination is seen to be essentially completed by 25 K, which is the temperature range in which thermal interconversion between rotoisomers of the photodissociated CO is observed in the photoproduct spectra of MbCO (*49*, *78*). This observation suggests that the temperature of rebinding in the TDS experiment is not governed by an activation enthalpy barrier at the heme iron but rather by the weak binding of the ligand in its docking site. Femtosecond IR spectroscopy of $Mb^{II}NO$ has also established the presence of two spectroscopically different but kinetically identical substates at ambient temperature (*25*). Apparently, the His-64 imidazole moiety does not sterically hinder NO access to the heme iron in either of the two spectroscopically distinguishable states.

The same set of TDS experiments was carried out on the ferrous and ferric forms of the mutant Mb samples. Instead of presenting these data as contour maps, we have plotted in Figure 6 the temperature dependence of the absorption changes in the bands of the heme-bound ligands integrated along the wavenumber axis. This representation provides an alternative, more compact way to display the temperature dependence of the rebinding reaction (but obscures spectral changes). For comparison, we have also included TDS data on MbCO. For the same photolysis protocol, it is obvious that the rebinding patterns are similar for ferrous and ferric NO preparations of the same mutant Mb. After 20-s illumination at 4 K, rebinding in wild-type Mb, I28W, H64V, and L104W occurs predominantly at ~15 K. In H64L, maximal recombination occurs at even lower temperatures; and a second process is faintly visible at ~30 K. In contrast, the rebinding peak is shifted to 35 K in V68Y $Mb^{III}NO$. After extended illumination, the temperature dependencies of the absorption changes in the bound-state bands of $Mb^{III}NO$ and $Mb^{II}NO$ are very similar (Figure 5G), with >80% of the photolyzed NO ligands rebinding in the population peaking at ~70 K. The photoproduct maps of the ferric and ferrous samples are essentially superimposable (Figure 5D, H).

NO Migration to Secondary Photoproduct Sites. There has been a long-standing debate about the determinants of the nonexponential geminate recombination in ferrous MbNO on picosecond time scales observed under physiological conditions. Petrich and co-workers, for instance, have proposed that protein relaxation, especially the iron-out-of-plane movement, dynamically increases the barrier against rebinding after ligand dissociation (*31*, *32*), as earlier suggested by Agmon and Hopfield (*85*). A similar dynamic model was invoked to explain the slowing of the flash photolysis kinetics of MbCO around 200 K (*86*, *87*). In the latter case, however, migration of CO to alternative docking sites was shown to be responsible for this effect (*18*, *88*), which raises the question if ligand migration could also be responsible for nonexponential rebinding in $Mb^{II}NO$ (*89*). On the basis of their recent temperature-dependent investigations of NO rebinding to mutant Mb samples, Ionascu et al. (*27*) explained the nonexponential process by recombination from a primary docking site and a more remote site. For $Mb^{III}NO$, EPR studies also gave evidence of two photoproduct sites at cryogenic temperatures (*90*).

Within 20-s illumination at 4 K, a rather small fraction of the NO ligands already escapes to another docking site with higher enthalpy barrier against rebinding (Figure 5E). This

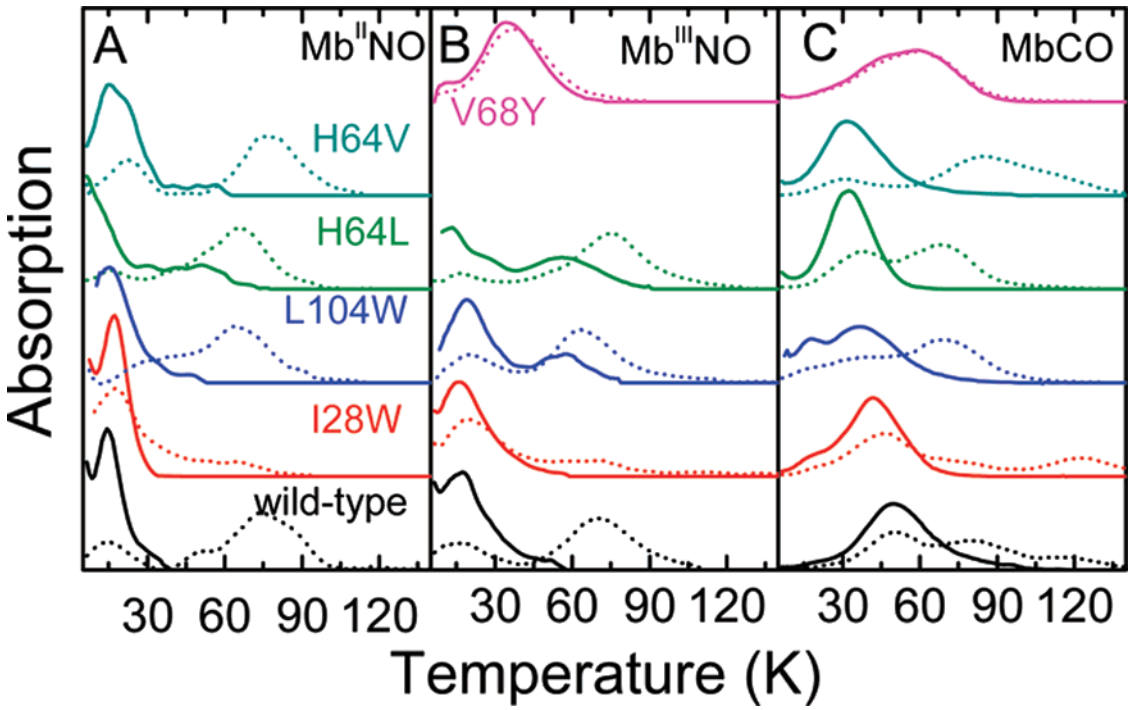

FIGURE 6: Integrated absorbance differences, $\int \Delta A(\nu) d\nu$, of Mb^{II}NO and Mb^{III}NO wild-type and mutant samples calculated from the TDS data as a function of temperature. Data on MbCO are included for comparison. TDS data were taken (solid lines) after brief illumination at 4 K and (dotted lines) after slow cooling from 160 to 4 K under constant illumination.

population can be enhanced by extended illumination. After slow cooling of ferrous and ferric wild-type MbNO from 160 to 4 K under continuous illumination, ~90% of all NO ligands are photolyzed and the majority is trapped in the secondary site, where they give rise to a doublet of stretching bands at 1865 and 1869 cm^{-1}, independent of the iron oxidation state (Figures 3 and 5). In MbCO, a third rebinding process occurs at ~120 K, which is entirely absent in the MbNO samples (Figure 6). Rebinding from this photoproduct peaks at ~70 K (Figure 6). The same intermediate is populated upon slow cooling of L104W MbNO (Figure 3C and 3F). In contrast, migration into the secondary site is markedly suppressed for mutant I28W, so that the predominant fraction of NO ligands still rebinds at ~15 K (Figure 6). Moreover, the photoproduct bands representing ligands at site B still comprise ~50% of the spectrum of I28W, whereas they are completely absent in wild-type Mb and L104W (Figure 3C). Ligand migration is totally absent in mutant V68Y; all ligands are trapped exclusively at the primary site for both illumination protocols (Figure 3E and 3F, Figure 6). By comparison with previous CO migration studies in Mb (*11*, *17*), these results enable us to unambiguously identify the secondary docking site with the Xe4 cavity (*38*): The Xe4 cavity is readily accessible to CO in mutant L104W, but partially blocked in I28W (*11*), whereas CO can migrate to the Xe1 site in I28W, but not in L104W, which has this cavity completely filled by the Trp-104 indole side chain. The introduction of an aromatic residue at position 68 is known to interfere with CO migration to both the Xe4 and Xe1 cavities (*17*). We also note that the ability of NO ligands to escape into the Xe4 cavity was suggested earlier by molecular dynamics simulations (*89*, *91*). The data in Figure 6 clearly indicate that, unlike CO, NO cannot be trapped in the Xe1 cavity at all, at least at cryogenic temperatures. This finding came as a surprise, as we had expected a similar migration behavior for NO and CO based on their similar molecular dimensions. As a matter of fact, NO is even slightly smaller as CO, which suggests that NO will experience less steric hindrance on its way from the Xe4 to the Xe1 cavity. However, we emphasize that our experiments can only detect a photoproduct population in a particular site (i) if a significant fraction of ligands migrates to this site instead of going to other, more easily accessible sites, and (ii) if sufficiently high free energy barriers exist that prevent fast return from this site. Our data indicate that NO is trapped in Xe4 in a different orientation than CO, which could give rise to a scenario in which the free energy barrier for migrating on to Xe1 is significantly higher than the one for returning to the distal pocket. Alternatively, the slightly smaller size of NO could lower the barrier for exiting Xe1 so that a significant photoproduct population cannot accumulate at low temperatures. By using time-resolved X-ray crystallography, we hope to clarify this interesting issue in the future.

NO Dynamics in the Xe4 Cavity. Temperature-dependent changes of the integrated absorption are not solely due to rebinding but may also reflect ligand reorientation at a particular site (*11*, *17*), ligand migration between sites (*36*), or librational dynamics of ligands covalently bound to the heme iron (*35*) or trapped in a docking site within the protein (*51*, *52*). In the photoproduct maps obtained after slow cooling of wild-type MbNO (Figure 5D,H), the bands at 1865 and 1869 cm^{-1}, which dominate most of the photoproduct spectra after slow-cool illumination, show characteristic features of ligand librations in a cavity. They exhibit a pronounced loss of intensity starting below 20 K, although rebinding from the secondary site represented by these bands becomes noticeable only above ~40 K, as seen from the contours in the bound-state maps (Figure 5C,G) and also in the integrated absorption changes (Figure 6). This behavior, which was also observed for the other mutant samples, was observed earlier for the photoproduct bands of the MbCO

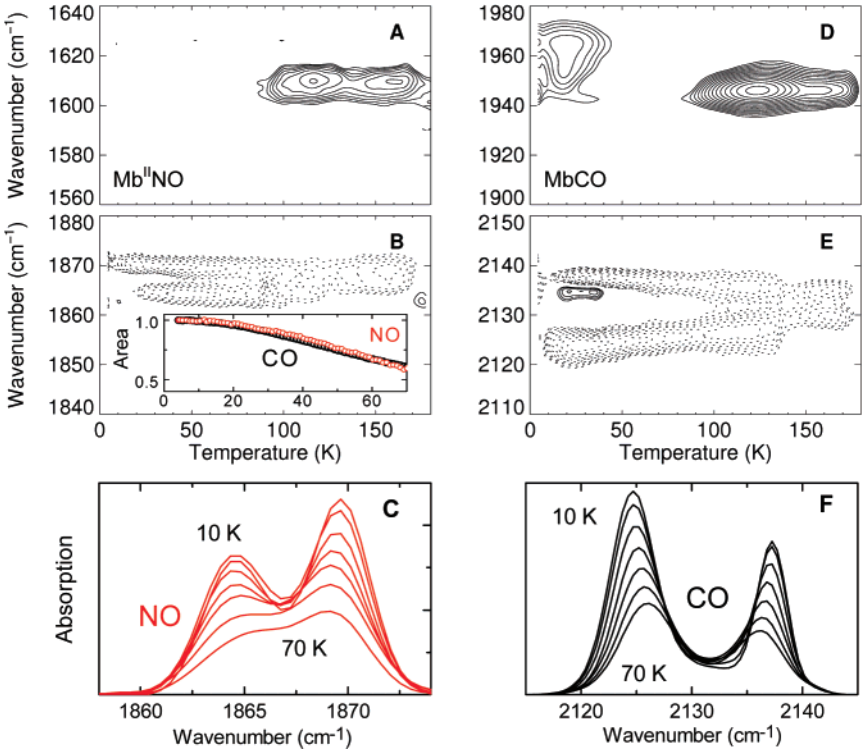

FIGURE 7: TDS data of L29W-S108L (left column) Mb^{II}NO and (right column) MbCO obtained after slow cooling from 160 to 4 K under continuous illumination. TDS contour maps in the bands of (A, D) heme-bound and (B, E) photodissociated NO and CO. Solid and dotted lines represent increasing and decreasing absorption, respectively; contours are spaced logarithmically. Inset in panel B: Normalized band areas of NO and CO as a function of temperature. FTIR absorbance difference spectra of (C) NO and (F) CO located in the Xe4 cavity, plotted from 10 to 70 K in 10-K intervals.

double mutant L29W-S108L, where it is particularly pronounced and was utilized to determine the internal electric field in the cavity (*51*, *52*). Therefore, we have studied the absorption changes in the NO photoproduct bands of this particular mutant after illumination during slow cooling from 160−4 K. The contour map in Figure 7A shows two discrete populations for NO rebinding, peaking at 115 and 160 K (Figure 7A,B). The two rebinding maxima are also seen for the CO-ligated species and have earlier been shown to arise from CO rebinding from the Xe4 cavity (Figure 7D,E), and the differences in the rebinding temperatures have been explained by a protein relaxation that leads to a collapse of the cavity volume (*51*).

NO ligands trapped in the Xe4 cavity of L29W-S108L Mb^{II}NO display stretching bands at 1864.7 and 1869.6 cm^{-1}. The Stark splitting of NO at 10 K (4.9 cm^{-1}) is significantly smaller than the one of CO (12.3 cm^{-1} (*52*)), as seen in Figure 7C,F. If we estimate, based on the previously published calculations (*81*, *82*), that the ratio of the Stark tuning rates between NO and CO is 0.8, it appears that the two ligands must be oriented differently within the cavity. Assuming opposite orientations, we have determined the angle θ between the CO dipole and the electric field vector (eq 1) in the Xe4 cavity as 29° (*51*). To explain the significantly smaller splitting in the case of NO (assuming that the electric field is identical), an angle θ as large as ~70° is required.

The TDS contours (Figure 7B) indicate a pronounced decrease of the NO photoproduct band areas between 10 and 70 K that is also clearly evident from the spectra (Figure 7C) and the normalized areas in the inset to Figure 7B. This loss in area is not related to rebinding, as can be seen from the absorption changes in the map of the heme-bound ligands that are only visible at temperatures above 80 K (Figure 7A). An additional experimental finding concerns the Stark splitting of the two bands, which decreases with increasing temperature (Figure 7C). Both effects were noticed earlier in the TDS maps of L29W-S108L MbCO (Figure 7D,E) and exploited to analyze the dynamics of CO in the Xe4 cavity in great detail (*51*, *52*). The temperature-dependent spectra can be described by a quantitative model that treats the CO ligand in the cavity as a two-dimensional oscillator, performing librational motions with a period of 1.3 ps. This motion was subsequently observed in the time domain by measuring the anisotropy decay in an ultrafast IR pump−probe experiment by Helbing et al. (*92*). The temperature-dependent effects on the NO and CO spectra are very similar (Figure 7C,F). The inset in Figure 7B shows that the decays of the integrated absorbances of NO and CO are essentially identical, which indicates the both ligands perform librational motions of comparable magnitude within the Xe4 cavity.

CONCLUSIONS

In this work, we have characterized conformational heterogeneity in both ligand-bound and photoproduct states of ferrous and ferric MbNO at cryogenic temperatures by using photolysis difference FTIR spectroscopy in combination with TDS. The His-64 imidazole side chain interacts with NO near the active site in different ways, depending on the particular protein conformation. Whereas His-64 makes a significant contribution to the rebinding enthalpy barrier in MbCO, it does not contribute to an enthalpy barrier to ligand binding in MbNO (except for the Mb^{III}NO conformation associated with the NO band at 1942 cm^{-1}),

so that the different conformation have identical rebinding properties. Whereas CO preferentially occupies the primary docking site B and sites C (Xe4 cavity) and D (Xe1 cavity) to a lesser extent in extended illumination experiments at cryogenic temperatures (*16*, *46*, *93*), NO readily escapes into the Xe4 cavity but cannot be trapped in Xe1.

Time-resolved crystallography and spectroscopy on MbCO at room temperature have disclosed that the internal cavities are not only pure packing defects or essential components of functional flexibility but provide transient binding sites and are parts of internal pathways for ligands migrating to and from the active site (*11*, *14*, *15*, *20*, *22*, *23*). Our present results with MbNO point to another physiological role of such a protein cavity: to function as a storage device of a macromolecular reactor, where MbO_2 and NO are transformed to ferric Mb and NO_3^-. This NO scavenging reaction of MbO_2 is very rapid (*8*), with estimated half-lives in the millisecond time range in the red muscle. By contrast, the oxidation reaction according to $2\ NO + O_2 \rightarrow 2\ NO_2$ in aqueous solution takes many seconds at the typical submicromolar concentrations of NO in the cell (*94*). The huge enhancement in reactivity seen for MbO_2 depends on the one hand on the superoxide character ($Fe^{3+-}O^{2-}$) acquired by O_2 bound to the heme iron (*95*); on the other hand, transient trapping of NO in the highly affine Xe4 cavity may considerably enhance the probability of the NO to encounter the 'activated' metal bound O_2^- (*7*, *10*) and, thereby, the *in situ* formation of the reaction intermediate peroxynitrite (*96*).

The pathophysiological significance of Mb as an NO scavenger has been substantiated by experiments carried out *in vivo* using Mb knock-out mice (*6*). Mb is crucial to the inactivation of NO and substantially determines the dose–response curve of the NO effects on coronary blood flow and cardiac contractility. The detailed chemistry of NO and its interactions with components of the cellular environment is complex and not yet well understood. Spectroscopic studies along the lines presented here can be useful for gaining further insight at the molecular level, as heme proteins are the key targets of NO in mammalian physiology.

ACKNOWLEDGMENT

We thank Uwe Theilen for help with protein expression and purification.

REFERENCES

1. Kim, S., Deinum, G., Gardner, M. T., Marletta, M. A., and Babcock, G. T. (1996) Distal Pocket Polarity in the Unusual Ligand Binding Site of Soluble Guanylate Cyclase: Implications for the Control of NO Binding, *J. Am. Chem. Soc. 118*, 8769–8770.
2. Boon, E. M., Huang, S. H., and Marletta, M. A. (2005) A molecular basis for NO selectivity in soluble guanylate cyclase, *Nat. Chem. Biol. 1*, 53–59.
3. Beltran, B., Mathur, A., Duchen, M. R., Erusalimsky, J. D., and Moncada, S. (2000) The effect of nitric oxide on cell respiration: A key to understanding its role in cell survival or death, *Proc. Natl. Acad. Sci. U.S.A. 97*, 14602–14607.
4. Gross, S. S., and Lane, P. (1999) Physiological reactions of nitric oxide and hemoglobin: a radical rethink, *Proc. Natl. Acad. Sci. U.S.A. 96*, 9967–9969.
5. Garry, D. J., Meeson, A., Yan, Z., and Williams, R. S. (2000) Life without myoglobin, *Cell Mol. Life Sci. 57*, 896–898.
6. Flögel, U., Merx, M. W., Gödecke, A., Decking, U. K., and Schrader, J. (2001) Myoglobin: A scavenger of bioactive NO, *Proc. Natl. Acad. Sci. U.S.A. 98*, 735–740.
7. Brunori, M. (2001) Nitric oxide moves myoglobin centre stage, *Trends Biochem. Sci. 26*, 209–210.
8. Eich, R. F., Li, T., Lemon, D. D., Doherty, D. H., Curry, S. R., Aitken, J. F., Mathews, A. J., Johnson, K. A., Smith, R. D., Phillips, G. N., Jr., and Olson, J. S. (1996) Mechanism of NO-induced oxidation of myoglobin and hemoglobin, *Biochemistry 35*, 6976–6983.
9. Herold, S., and Röck, G. (2003) Reactions of deoxy-, oxy-, and methemoglobin with nitrogen monoxide. Mechanistic studies of the S-nitrosothiol formation under different mixing conditions, *J. Biol. Chem. 278*, 6623–6634.
10. Brunori, M. (2001) Nitric oxide, cytochrome-c oxidase and myoglobin, *Trends Biochem. Sci. 26*, 21–23.
11. Nienhaus, K., Deng, P., Kriegl, J. M., and Nienhaus, G. U. (2003) Structural Dynamics of Myoglobin: The Effect of Internal Cavities on Ligand Migration and Binding, *Biochemistry 42*, 9647–9658.
12. Dantsker, D., Samuni, U., Friedman, A. J., Yang, M., Ray, A., and Friedman, J. M. (2002) Geminate rebinding in trehalose-glass embedded myoglobins reveals residue-specific control of intramolecular trajectories, *J. Mol. Biol. 315*, 239–251.
13. Samuni, U., Dantsker, D., Khan, I., Friedman, A. J., Peterson, E., and Friedman, J. M. (2002) Spectroscopically and kinetically distinct conformational populations of sol-gel-encapsulated carbonmonoxy myoglobin. A comparison with hemoglobin, *J. Biol. Chem. 277*, 25783–25790.
14. Scott, E. E., and Gibson, Q. H. (1997) Ligand migration in sperm whale myoglobin, *Biochemistry 36*, 11909–11917.
15. Scott, E. E., Gibson, Q. H., and Olson, J. S. (2001) Mapping the pathways for O_2 entry into and exit from myoglobin, *J. Biol. Chem. 276*, 5177–5188.
16. Nienhaus, K., Deng, P., Kriegl, J. M., and Nienhaus, G. U. (2003) Structural Dynamics of Myoglobin: Spectroscopic and Structural Characterization of Ligand Docking Sites in Myoglobin Mutant L29W, *Biochemistry 42*, 9633–9646.
17. Nienhaus, K., Deng, P., Olson, J. S., Warren, J. J., and Nienhaus, G. U. (2003) Structural Dynamics of Myoglobin: Ligand Migration and Binding in Valine 68 Mutants, *J. Biol. Chem. 278*, 42532–42544.
18. Ostermann, A., Waschipky, R., Parak, F. G., and Nienhaus, G. U. (2000) Ligand binding and conformational motions in myoglobin, *Nature 404*, 205–208.
19. Brunori, M., Vallone, B., Cutruzzola, F., Travaglini-Allocatelli, C., Berendzen, J., Chu, K., Sweet, R. M., and Schlichting, I. (2000) The role of cavities in protein dynamics: crystal structure of a photolytic intermediate of a mutant myoglobin, *Proc. Natl. Acad. Sci. U.S.A. 97*, 2058–2063.
20. Bourgeois, D., Vallone, B., Schotte, F., Arcovito, A., Miele, A. E., Sciara, G., Wulff, M., Anfinrud, P., and Brunori, M. (2003) Complex landscape of protein structural dynamics unveiled by nanosecond Laue crystallography, *Proc. Natl. Acad. Sci. U.S.A. 100*, 8704–8709.
21. Hummer, G., Schotte, F., and Anfinrud, P. A. (2004) Unveiling functional protein motions with picosecond x-ray crystallography and molecular dynamics simulations, *Proc. Natl. Acad. Sci. U.S.A. 101*, 15330–15334.
22. Schmidt, M., Nienhaus, K., Pahl, R., Krasselt, A., Anderson, S., Parak, F., Nienhaus, G. U., and Srajer, V. (2005) Ligand migration pathway and protein dynamics in myoglobin: a time-resolved crystallographic study on L29W MbCO, *Proc. Natl. Acad. Sci. U.S.A. 102*, 11704–11709.
23. Schotte, F., Lim, M., Jackson, T. A., Smirnov, A. V., Soman, J., Olson, J. S., Phillips, G. N., Jr., Wulff, M., and Anfinrud, P. A. (2003) Watching a protein as it functions with 150-ps time-resolved x-ray crystallography, *Science 300*, 1944–1947.
24. Miller, L. M., Pedraza, A. J., and Chance, M. R. (1997) Identification of conformational substates involved in nitric oxide binding to ferric and ferrous myoglobin through difference Fourier transform infrared spectroscopy (FTIR), *Biochemistry 36*, 12199–12207.
25. Kim, S., Jin, G., and Lim, M. (2004) Dynamics of Geminate Recombination of NO with Myoglobin in Aqueous Solution Probed by Femtosecond Mid-IR Spectroscopy, *J. Phys. Chem. B 108*, 20366–20375.
26. Kim, S., and Lim, M. (2005) Protein conformation-induced modulation of ligand binding kinetics: a femtosecond mid-IR study of nitric oxide binding trajectories in myoglobin, *J. Am. Chem. Soc. 127*, 8908–8909.
27. Ionascu, D., Gruia, F., Ye, X., Yu, A., Rosca, F., Beck, C., Demidov, A., Olson, J. S., and Champion, P. M. (2005) Tem-

perature-dependent studies of NO recombination to heme and heme proteins, *J. Am. Chem. Soc. 127*, 16921−16934.
28. Petrich, J. W., Poyart, C., and Martin, J. L. (1988) Photophysics and reactivity of heme proteins: a femtosecond absorption study of hemoglobin, myoglobin, and protoheme, *Biochemistry 27*, 4049−4060.
29. Olson, J. S., and Phillips, G. N., Jr. (1996) Kinetic pathways and barriers for ligand binding to myoglobin, *J. Biol. Chem. 271*, 17593−17596.
30. Ye, X., Demidov, A., and Champion, P. M. (2002) Measurements of the photodissociation quantum yields of MbNO and MbO_2 and the vibrational relaxation of the six-coordinate heme species, *J. Am. Chem. Soc. 124*, 5914−5924.
31. Petrich, J. W., Lambry, J. C., Balasubramanian, S., Lambright, D. G., Boxer, S. G., and Martin, J. L. (1994) Ultrafast measurements of geminate recombination of NO with site-specific mutants of human myoglobin, *J. Mol. Biol. 238*, 437−444.
32. Petrich, J. W., Lambry, J. C., Kuczera, K., Karplus, M., Poyart, C., and Martin, J. L. (1991) Ligand binding and protein relaxation in heme proteins: a room temperature analysis of NO geminate recombination, *Biochemistry 30*, 3975−3987.
33. Cao, W., Christian, J. F., Champion, P. M., Rosca, F., and Sage, J. T. (2001) Water penetration and binding to ferric myoglobin, *Biochemistry 40*, 5728−5737.
34. Deng, P., Nienhaus, K., Palladino, P., Olson, J. S., Blouin, G., Moens, L., Dewilde, S., Geuens, E., and Nienhaus, G. U. (2007) Transient ligand docking sites in Cerebratulus lacteus mini-hemoglobin, *Gene 398*, 208−223.
35. Nienhaus, K., Maes, E. M., Weichsel, A., Montfort, W. R., and Nienhaus, G. U. (2004) Structural dynamics controls nitric oxide affinity in nitrophorin 4, *J. Biol. Chem. 279*, 39401−39407.
36. Lamb, D. C., Nienhaus, K., Arcovito, A., Draghi, F., Miele, A. E., Brunori, M., and Nienhaus, G. U. (2002) Structural dynamics of myoglobin: ligand migration among protein cavities studied by Fourier transform infrared/temperature derivative spectroscopy, *J. Biol. Chem. 277*, 11636−11644.
37. Nienhaus, K., and Nienhaus, G. U. (2007) Ligand Dynamics in Heme Proteins Observed by Fourier Transform Infrared Spectroscopy at Cryogenic Temperatures, *Methods Enzymol.*, in press.
38. Tilton, R. F., Jr., Kuntz, I. D., Jr., and Petsko, G. A. (1984) Cavities in proteins: structure of a metmyoglobin-xenon complex solved to 1.9 Å, *Biochemistry 23*, 2849−2857.
39. Nienhaus, G. U., and Nienhaus, K. (2002) Infrared Study of Carbon Monoxide Migration among Internal Cavities of Myoglobin Mutant L29W, *J. Biol. Phys. 28*, 163−172.
40. Springer, B. A., and Sligar, S. G. (1987) High-level expression of sperm whale myoglobin in Escherichia coli, *Proc. Natl. Acad. Sci. U.S.A. 84*, 8961−8965.
41. Krezel, A., and Bal, W. (2004) A formula for correlating pKa values determined in D_2O and H_2O, *J. Inorg. Biochem. 98*, 161−166.
42. Douzou, P. (1977) *Cryobiochemistry*, Academic Press, New York.
43. Mourant, J. R., Braunstein, D. P., Chu, K., Frauenfelder, H., Nienhaus, G. U., Ormos, P., and Young, R. D. (1993) Ligand binding to heme proteins: II. Transitions in the heme pocket of myoglobin, *Biophys. J. 65*, 1496−1507.
44. Nienhaus, K., Lamb, D. C., Deng, P., and Nienhaus, G. U. (2002) The Effect of Ligand Dynamics on Heme Electronic Transition Band III in Myoglobin, *Biophys. J. 82*, 1059−1067.
45. Berendzen, J., and Braunstein, D. (1990) Temperature-derivative spectroscopy: a tool for protein dynamics, *Proc. Natl. Acad. Sci. U.S.A. 87*, 1−5.
46. Nienhaus, G. U., Mourant, J. R., Chu, K., and Frauenfelder, H. (1994) Ligand binding to heme proteins: the effect of light on ligand binding in myoglobin, *Biochemistry 33*, 13413−13430.
47. Austin, R. H., Beeson, K. W., Eisenstein, L., Frauenfelder, H., and Gunsalus, I. C. (1975) Dynamics of ligand binding to myoglobin, *Biochemistry 14*, 5355−5373.
48. Ehrenstein, D., and Nienhaus, G. U. (1992) Conformational substates in azurin, *Proc. Natl. Acad. Sci. U.S.A. 89*, 9681−9685.
49. Alben, J. O., Beece, D., Bowne, S. F., Doster, W., Eisenstein, L., Frauenfelder, H., Good, D., McDonald, J. D., Marden, M. C., Moh, P. P., Reinisch, L., Reynolds, A. H., Shyamsunder, E., and Yue, K. T. (1982) Infrared spectroscopy of photodissociated carboxymyoglobin at low temperatures, *Proc. Natl. Acad. Sci. U.S.A. 79*, 3744−3748.
50. Chu, K., Ernst, R. M., Frauenfelder, H., Mourant, J. R., Nienhaus, G. U., and Philipp, R. (1995) Light-induced and thermal relaxation in a protein, *Phys. Rev. Lett. 74*, 2607−2610.
51. Lehle, H., M., K. J., Nienhaus, K., Deng, P., Fengler, S., and Nienhaus, G. U. (2005) Probing Electric Fields in Protein Cavities by Using the Vibrational Stark Effect of Carbon Monoxide, *Biophys. J. 88*, 1978−1990.
52. Kriegl, J. M., Nienhaus, K., Deng, P., Fuchs, J., and Nienhaus, G. U. (2003) Ligand dynamics in a protein internal cavity, *Proc. Natl. Acad. Sci. U.S.A. 100*, 7069−7074.
53. Ansari, A., Berendzen, J., Braunstein, D., Cowen, B. R., Frauenfelder, H., Hong, M. K., Iben, I. E., Johnson, J. B., Ormos, P., Sauke, T. B., and et al. (1987) Rebinding and relaxation in the myoglobin pocket, *Biophys. Chem. 26*, 337−355.
54. Braunstein, D. P., Chu, K., Egeberg, K. D., Frauenfelder, H., Mourant, J. R., Nienhaus, G. U., Ormos, P., Sligar, S. G., Springer, B. A., and Young, R. D. (1993) Ligand binding to heme proteins: III. FTIR studies of His-E7 and Val-E11 mutants of carbonmonoxymyoglobin, *Biophys. J. 65*, 2447−2454.
55. Li, T., Quillin, M. L., Phillips, G. N., Jr., and Olson, J. S. (1994) Structural determinants of the stretching frequency of CO bound to myoglobin, *Biochemistry 33*, 1433−1446.
56. Müller, J. D., McMahon, B. H., Chien, E. Y., Sligar, S. G., and Nienhaus, G. U. (1999) Connection between the taxonomic substates and protonation of histidines 64 and 97 in carbonmonoxy myoglobin, *Biophys. J. 77*, 1036−1051.
57. Kushkuley, B., and Stavrov, S. S. (1997) Theoretical study of the electrostatic and steric effects on the spectroscopic characteristics of the metal-ligand unit of heme proteins. 2. C-O vibrational frequencies, ^{17}O isotropic chemical shifts, and nuclear quadrupole coupling constants, *Biophys. J. 72*, 899−912.
58. Yang, F., and Phillips, G. N., Jr. (1996) Crystal structures of CO-, deoxy- and met-myoglobins at various pH values, *J. Mol. Biol. 256*, 762−774.
59. Tian, W. D., Sage, J. T., and Champion, P. M. (1993) Investigations of ligand association and dissociation rates in the "open" and "closed" states of myoglobin, *J. Mol. Biol. 233*, 155−166.
60. Vojtechovsky, J., Chu, K., Berendzen, J., Sweet, R. M., and Schlichting, I. (1999) Crystal structures of myoglobin-ligand complexes at near-atomic resolution, *Biophys. J. 77*, 2153−2174.
61. Johnson, J. B., Lamb, D. C., Frauenfelder, H., Müller, J. D., McMahon, B., Nienhaus, G. U., and Young, R. D. (1996) Ligand binding to heme proteins. VI. Interconversion of taxonomic substates in carbonmonoxymyoglobin, *Biophys. J. 71*, 1563−1573.
62. Ray, G. B., Li, X.-Y., Ibers, J. A., Sessler, J. L., and Spiro, G. S. (1994) How far can proteins bend the FeCO unit, *J. Am. Chem. Soc. 116*, 162−176.
63. Vogel, K. M., Kozlowski, P. M., Zgierski, M. Z., and Spiro, T. G. (1999) Determinants of the FeXO (X = C, N, O) vibrational frequencies in heme adducts from experiment and density functional theory, *J. Am. Chem. Soc. 121*, 9915−9921.
64. Coyle, C. M., Vogel, K. M., Rush, T. S., 3rd, Kozlowski, P. M., Williams, R., Spiro, T. G., Dou, Y., Ikeda-Saito, M., Olson, J. S., and Zgierski, M. Z. (2003) FeNO structure in distal pocket mutants of myoglobin based on resonance Raman spectroscopy, *Biochemistry 42*, 4896−4903.
65. Park, E. S., and Boxer, S. G. (2002) Origins of the sensitivity of molecular vibrations to electric fields: Carbonyl and Nitrosyl stretches in model compounds and proteins, *J. Phys. Chem. B 106*, 5800−5806.
66. Tomita, T., Hirota, S., Ogura, T., Olson, J. S., and Kitagawa, T. (1999) Resonance Raman Investigations of Fe-N-O Structure Nitrosylheme in Myoglobin and Its Mutants, *J. Phys. Chem. B 103*, 7044−7054.
67. Park, E. S., Thomas, M. R., and Boxer, S. G. (2000) Vibrational Stark Spectroscopy of NO bound to Heme: Effects of Protein Electrostatic fields on the NO Stretch Frequency, *J. Am. Chem. Soc. 122*, 12297−12303.
68. Hoffman, B. M., and Gibson, Q. H. (1978) On the photosensitivity of liganded hemoproteins and their metal-substituted analogues, *Proc. Natl. Acad. Sci. U.S.A. 75*, 21−25.
69. Martin, J. L., and Vos, M. H. (1994) Femtosecond measurements of geminate recombination in heme proteins, *Methods Enzymol. 232*, 416−430.
70. Nutt, D. R., and Meuwly, M. (2007) Ferric and Ferrous Iron in Nitroso-Myoglobin: Computer Simulations of Stable and Metastable States and Their Infrared Spectra, *Chemphyschem 8*, 527−536.
71. Nutt, D. R., Karplus, M., and Meuwly, M. (2005) Potential energy surface and molecular dynamics of MbNO: existence of an unsuspected FeON minimum, *J. Phys. Chem. B 109*, 21118−21125.

72. Cheng, L., Novozhilova, I., Kim, C., Kovalevsky, A., Bagley, K. A., Coppens, P., and Richter-Addo, G. B. (2000) First Observation of Photoinduced Nitrosyl Linkage Isomers of Iron Nitrosyl Porphyrins, *J. Am. Chem. Soc. 122*, 7142−7143.
73. Hartmann, H., Zinser, S., Komninos, P., Schneider, R. T., Nienhaus, G. U., and Parak, F. (1996) X-ray structure determination of a metastable state of carbonmonoxy myoglobin after photodissociation, *Proc. Natl. Acad. Sci. U.S.A. 93*, 7013−7016.
74. Lim, M., Jackson, T. A., and Anfinrud, P. A. (1997) Ultrafast rotation and trapping of carbon monoxide dissociated from myoglobin, *Nat. Struct. Biol. 4*, 209−214.
75. Schlichting, I., Berendzen, J., Phillips, G. N., Jr., and Sweet, R. M. (1994) Crystal structure of photolysed carbonmonoxy-myoglobin, *Nature 371*, 808−812.
76. Teng, T. Y., Srajer, V., and Moffat, K. (1994) Photolysis-induced structural changes in single crystals of carbonmonoxy myoglobin at 40 K, *Nat. Struct. Biol. 1*, 701−705.
77. Lim, M., Jackson, T. A., and Anfinrud, P. A. (1995) Binding of CO to myoglobin from a heme pocket docking site to form nearly linear Fe-C-O, *Science 269*, 962−966.
78. Nienhaus, K., Olson, J. S., Franzen, S., and Nienhaus, G. U. (2005) The origin of Stark splitting in the initial photoproduct state of MbCO, *J. Am. Chem. Soc. 127*, 40−41.
79. Bredenbeck, J., Helbing, J., Nienhaus, K., Nienhaus, G. U., and Hamm, P. (2007) Multidimensional Ultrafast Spectroscopy Special Feature: Protein ligand migration mapped by nonequilibrium 2D-IR exchange spectroscopy, *Proc. Natl. Acad. Sci. U.S.A. 104*, 14243−14248.
80. Park, E. S., Andrews, S. S., Hu, R. B., and Boxer, S. G. (1999) Vibrational Stark spectroscopy in proteins: A probe and calibration for electrostatic fields, *J. Phys. Chem. B 103*, 9813−9817.
81. Dalosto, S. D., Vanderkooi, J. M., and Sharp, K. A. (2004) Vibrational Stark Effects on Carbonyl, Nitrile, and Nitrosyl Compounds Including Heme Ligands, CO, CN, and NO, Studied with Density Functional Theory *J. Phys. Chem. B 108*, 6450−6457.
82. Mankoo, P. K., and Keyes, T. (2006) Classical Molecular Electrostatics: Recognition of Ligands in Proteins and the Vibrational Stark Effect, *J. Phys. Chem. B 110*, 25074−25079.
83. Engler, N., Prusakov, V., Ostermann, A., and Parak, F. G. (2003) A water network within a protein: temperature-dependent water ligation in H64V-metmyoglobin and relaxation to deoxymyoglobin, *Eur. Biophys. J. 31*, 595−607.
84. Ho, W. C., Ozier, I., Cramb, D. T., and Gerry, M. C. L. (1991) Diode Laser Spectroscopy of the Vibrational Fundamental of NO^+, *J. Mol. Spectrosc. 149*, 559−561.
85. Agmon, N., and Hopfield, J. J. (1983) CO binding to heme proteins: A model for barrier height distributions and slow conformational changes, *J. Chem. Phys. 79*, 2042−2053.
86. Steinbach, P. J., Ansari, A., Berendzen, J., Braunstein, D., Chu, K., Cowen, B. R., Ehrenstein, D., Frauenfelder, H., Johnson, J. B., Lamb, D. C., Luck, S., Mourant, J. R., Nienhaus, G. U., Ormos, P., Philipp, R., Xie, A., and Young, R. D. (1991) Ligand binding to heme proteins: connection between dynamics and function, *Biochemistry 30*, 3988−4001.
87. Frauenfelder, H., Nienhaus, G. U., and Johnson, J. B. (1991) Rate Processes in Proteins, *Ber. Bunsenges. Phys. Chem. 95*, 272−278.
88. Dantsker, D., Roche, C., Samuni, U., Blouin, G., Olson, J. S., and Friedman, J. M. (2005) The position 68(E11) side chain in myoglobin regulates ligand capture, bond formation with heme iron, and internal movement into the xenon cavities, *J. Biol. Chem. 280*, 38740−38755.
89. Carlson, M. L., Regan, R., Elber, R., Li, H., Phillips, G. N., Jr., Olson, J. S., and Gibson, Q. H. (1994) Nitric oxide recombination to double mutants of myoglobin: role of ligand diffusion in a fluctuating heme pocket, *Biochemistry 33*, 10597−10606.
90. Hori, H., Masuya, F., Dou, Y., and Ikeda-Saito, M. (2000) EPR studies on the photoinduced intermediates of NO complexes in recombinant ferric-Mb trapped at low temperatures, *J. Inorg. Biochem. 82*, 181−187.
91. Nutt, D. R., and Meuwly, M. (2006) Studying reactive processes with classical dynamics: rebinding dynamics in MbNO, *Biophys. J. 90*, 1191−1201.
92. Helbing, J., Nienhaus, K., Nienhaus, G. U., and Hamm, P. (2005) Restricted Rotational Motion of CO in a Protein Internal Cavity: Evidence for Non-Separating Correlation Functions from IR Pump-Probe Spectroscopy, *J. Chem. Phys. 122*, 124505.
93. Nienhaus, G. U., Chu, K., and Jesse, K. (1998) Structural heterogeneity and ligand binding in carbonmonoxy myoglobin crystals at cryogenic temperatures, *Biochemistry 37*, 6819−6823.
94. Ford, P. C., Wink, D. A., and Stanbury, D. M. (1993) Autoxidation kinetics of aqueous nitric oxide, *FEBS Lett. 326*, 1−3.
95. Weiss, J. J. (1964) Nature of the Iron-Oxygen Bond in Oxyhaemoglobin, *Nature 203*, 182−183.
96. Herold, S. (1999) Kinetic and spectroscopic characterization of an intermediate peroxynitrite complex in the nitrogen monoxide induced oxidation of oxyhemoglobin, *FEBS Lett. 443*, 81−84.

BI701935V